Femtosecond Laser-Induced Electron Emission from Nanodiamond-Coated Tungsten Needle Tips

A. Tafel,* S. Meier, J. Ristein, and P. Hommelhoff
Department of Physics, Friedrich-Alexander-Universität Erlangen-Nürnberg, Staudtstraße 1, D-91058 Erlangen, Germany

(Received 13 March 2019; revised manuscript received 19 July 2019; published 2 October 2019)

We present femtosecond laser-induced electron emission from nanodiamond-coated tungsten tips. Based on the shortness of the femtosecond laser pulses, electrons can be photoexcited for wavelengths from the infrared (1932 nm) to the ultraviolet (235 nm) because multiphoton excitation becomes efficient over the entire spectral range. Depending on the laser wavelength, we find different dominant emission channels identified by the number of photons needed to emit electrons. Based on the band alignment between tungsten and nanodiamond, the relevant emission channels can be identified as specific transitions in diamond and its graphitic boundaries. It is the combination of the character of initial and final states (i.e., bulk or surface-near, direct or indirect excitation in the diamond band structure), the number of photons providing the excitation energy, and the peak intensity of the laser pulses that determines the dominant excitation channel for photoemission. A specific feature of the hydrogen-terminated nanodiamond coating is its negative electron affinity that significantly lowers the work function and enables efficient emission from the conduction band minimum into vacuum without an energy barrier. Emission is stable for bunch charges of up to 400 electrons per laser pulse. We infer a normalized emittance of <0.20 nm rad and a normalized peak brightness of $>1.2 \times 10^{12}$ A m^{-2} sr^{-1}. The properties of these tips are encouraging for their use as laser-triggered electron sources in applications such as ultrafast electron microscopy as well as diffraction and novel photonics-based laser accelerators.

DOI: 10.1103/PhysRevLett.123.146802

Tip-shaped cathodes are among the most commonly used electron sources in electron microscopy due to their ability to provide a high quality beam. Typical materials are zirconia in common Schottky type emitters and lanthanum hexaboride because of their low work function, as well as tungsten due to the easy fabrication of sharp tips ideally suited for (cold) field emission [1]. Most of the commonly used emitters are operated under ultrahigh vacuum conditions in the 10^{-8}–10^{-9} Pa regime to minimize bombardment with ionized gas and adsorption on the emitter surface. Furthermore, they are heated for thermal enhancement of the emission or to achieve stable operation due to reduced adsorption.

Over the last decades, ultrafast electron microscopy has emerged [2–4]. Until today, emitters, which were designed for dc operation, are also used in ultrafast mode. In the latter case, the cathode is typically triggered by femtosecond laser pulses resulting in femto- to picosecond electron pulses [5–10]. One of the major drawbacks of these laser-triggered electron sources is the continuous decrease of emission current over time [5,9,10], which is attributed to laser-induced changes at the emitter surface. Femtosecond laser-induced photoemission from tip-shaped cathodes has been extensively studied for the materials of tungsten [11–16], gold [17–19], silver [20], hafnium carbide [21], and carbon nanotubes [22,23]. Pulsed photoemission from single crystal diamond tips has been investigated with nanosecond pulses [24]. Femtosecond photoemission from tip-shaped heterostructures offers promising opportunities yet to be discovered.

Diamond is one of the most robust materials due to its exceptional chemical inertness, mechanical strength, and thermal conductivity. Nanocrystalline diamond (NCD) is a good electron emitter, especially if the surface exhibits negative electron affinity (NEA) [25]. The graphitic grain boundaries in this composite material provide electrical conductivity, and the low work function of the diamond matrix that goes along with the NEA lowers the surface energy barrier for the electrons, even if they originate from the graphitic parts [25]. NEA is also known to boost the photoelectron yield due to fundamental absorption, i.e., optical excitation across the band gap: electrons photoexcited into the diamond conduction band can be emitted into vacuum without any barrier after migration to the surface [26,27]. The electron affinity of hydrogen-terminated diamond is as low as -1.3 eV for both main crystallographic surfaces (100) [28] and (111) [29].

The combination of high beam quality from tip-shaped photocathodes with the mechanical strength and the low work function of hydrogen-terminated diamond promises a robust and high-brightness photocathode. Here, we present the first photoemission results from a tip-shaped semiconductor/metal heterostructure—diamond-coated tungsten tips—triggered with femtosecond laser pulses, and

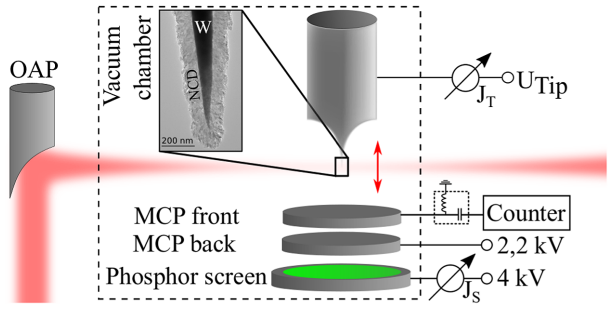

FIG. 1. Experimental setup. The laser is focused onto the diamond-coated tungsten tip with an off-axis parabolic mirror (OAP). The inset shows a transmission electron micrograph of the nanodiamond-coated tungsten tip. A voltage clearly below the dc field emission threshold is applied between the tip and the microchannel plate (MCP) to accelerate electrons towards the MCP. See text for details.

we characterize the underlying photoemission physics by identifying various emission channels. We define an emission channel as the combination of photon energy and energy states involved in the photoemission process of electrons.

To obtain the nanodiamond-coated tips, 100 μm diameter tungsten wire is electrochemically etched, resulting in a tip with a typical apex radius of roughly 10 nm. The freshly etched tip is dip seeded in nanodiamond suspension and dry blown with pressurized nitrogen. NCD is grown on the seeded tips with microwave-enhanced chemical vapor deposition, resulting in a dense film of hydrogen-terminated nanocrystalline diamond with negative electron affinity covering the tungsten surface (Fig. 1 inset). A thin layer of tungsten carbide (WC) is expected to be formed at the diamond-tungsten interface [30]. Samples used in this work have apex radii between 60 and 200 nm, including the diamond coating. Details of the fabrication process and a structural characterization of the tips are published elsewhere [31].

The so-fabricated tips are mounted in an ultrahigh vacuum chamber with a base pressure of 1×10^{-7} Pa. Femtosecond laser pulses are focused at the tip with the help of a 51 mm diameter off-axis parabolic mirror with a 152 mm focal length outside of the vacuum chamber, resulting in a measured spot radius of 3.8 μm at 512 nm ($1/e^2$ intensity radius). The employed commercial laser system consists of a regeneratively amplified Ti:Sa oscillator (1 kHz repetition rate, 80 fs pulse duration), an optical parametric amplifier, and a stage for second harmonic and sum-frequency generation. Additionally, a Ti:Sa oscillator (780 nm, 80 MHz, 6 fs) is used for long-term stability measurements. We apply a negative voltage below 50% of the dc field emission threshold (400–2000 V, depending on the individual tip). Due to the dielectric surface with a small work function of 2.8 eV [Eq. (2)], the Schottky reduction is lower as compared to metal tips and is neglected here. The dc field is chosen low enough that photon-assisted field emission does not occur: only multiphoton emission. The laser pulses are linearly polarized parallel to the tip axis. Photoemitted electrons are detected with a microchannel plate (MCP) with a grounded front plate. For bunch charges below one electron per laser pulse, we count detection events on the MCP; above one electron per pulse, we measure the calibrated MCP screen current; and for large average currents at high repetition rates, we are able to additionally measure the current through the tip.

In order to identify the different contributions to the photoelectron current J, we have measured its dependence on the peak intensity I_p. Due to the high I_p of the femtosecond laser pulses, optical excitation is not limited to one-photon absorption processes as the multiphoton absorption becomes efficient. The dependence of the photoelectron current J on I_p is expected to be a sum of power law contributions:

$$J = \sum_n^\infty a_n I_p^n, \tag{1}$$

where n reflects the number of photons necessary to provide the excitation energy, and a_n is the corresponding coefficient for the specific emission channel. Often, one channel is dominant; hence, the slope of $\log(J)$ vs $\log(I_p)$ directly reveals the photon order n. If more than one channel is involved with comparable strength, the linearized slope is a noninteger and is called effective nonlinearity. Depending on the photon energy and laser intensity, different emission channels can become dominant. We show the power dependence of the photoelectron current at wavelengths of 1932, 512, and 256 nm in Fig. 2. For 1932 nm, we find an integer slope of 5.0, indicating a single dominating emission channel with five photons. At 512 nm, the plot shows an effective nonlinearity of 3.4. This is indicative for two channels with photon orders of 3 and 4 contributing. At 256 nm, we observe a transition from photon order one at low intensities to photon order two at high intensities.

In the UV (235–350 nm), we have investigated the wavelength dependence of the effective nonlinearity in more detail. Figure 3(a) shows the $\log(J)$ vs $\log(I_p)$ plot for 235, 260, and 350 nm. We find effective nonlinearities of 1.1, 1.4, and 2.0, respectively. Again, this reflects the transition of the dominant emission channel from first to second order. Note that we do not observe a transition in the power dependence directly in contrast to Fig. 2(b). This is due to the restricted pulse energy range in Fig. 3. The effective nonlinearities for all wavelengths in the UV are summarized in Fig. 3(b), confirming the transition mentioned above.

For the interpretation of the data, we sketch the energy states relevant for this work in Fig. 4. Five junctions between W/WC, diamond, vacuum, and the graphitic grain boundaries (called graphite in Fig. 4) are formed.

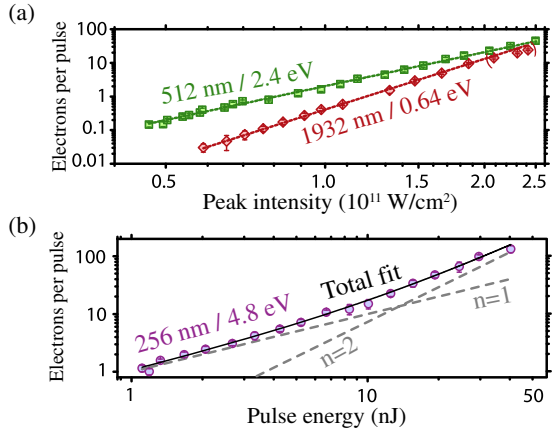

FIG. 2. (a) Photoemission at 1932 nm (red diamonds) and 512 nm (green squares), with slopes of 5.0 (red dashed line, with last three data points not included due to potential saturation effects) and 3.4 (green dashed line). (b) Transition from one- to two-photon emission at 256 nm. Gray dashed lines are corresponding contributions, and the solid black line is the sum of the two contributions. Note that we used pulse energy instead of peak intensity in Fig. 2(b) because we could not measure the laser spot size in the UV.

Diamond forms Schottky junctions with graphite and W/WC with Schottky barriers of $E_{B,G} = 1.4$ eV [32] and $E_{B,\mathrm{W/WC}} = 1.2$ eV [33], respectively. As the sample surface only consists of diamond grains and their graphitic boundaries, the junctions of diamond-vacuum and graphite-vacuum are the relevant ones for electron emission into vacuum. In a heterosystem involving metallic (W/WC and, in a good approximation, the half-metal graphite) and semiconducting (diamond) components, the Fermi level in the semiconductor relative to the valence band maximum (VBM) is identical to the Schottky barrier height as long as the dimensions of the semiconducting parts are much below

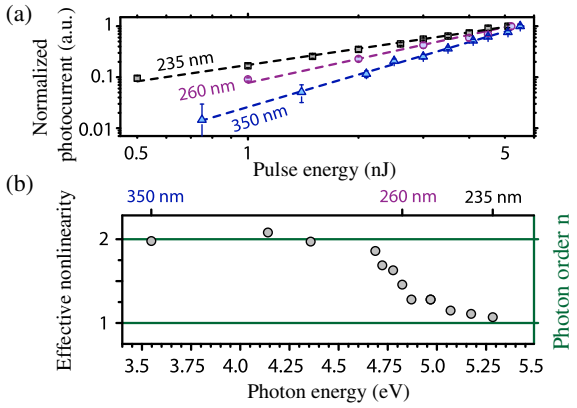

FIG. 3. Power scaling in the UV with transition from one- to two-photon emission as the dominant channel. (a) Data at 235 (black squares), 260 (violet circles), and 350 nm (blue triangles) with effective nonlinearities of 1.1, 1.4, and 2.0, respectively. (b) Effective nonlinearity vs Photon energy with a gradual transition from $n = 1$ to $n = 2$ at roughly 4.8 eV.

the Debye length of the semiconductor. This is certainly the case for the diamond grains. We expect $E_{B,G}$ to dominate at the diamond surface because the average grain size (approximately 20 nm) is smaller than the thickness of the diamond film. Consequently, the Fermi level is $E_{B,\mathrm{W/WC}} = 1.2$ eV above the VBM at the back contact and $E_{B,G} = 1.4$ eV above the VBM at the free surface [see Fig. 4(a)]. The work function Φ is defined as the energy difference between the vacuum level and the surface Fermi level. Graphite has a work function of 4.7 eV [34], whereas the work function of diamond depends on the electron affinity χ, and $E_{B,G}$ and results in

$$\Phi_{\mathrm{dia}} = E_g - E_{B,G} + \chi = (5.5 - 1.4 - 1.3)\ \mathrm{eV} = 2.8\ \mathrm{eV}, \tag{2}$$

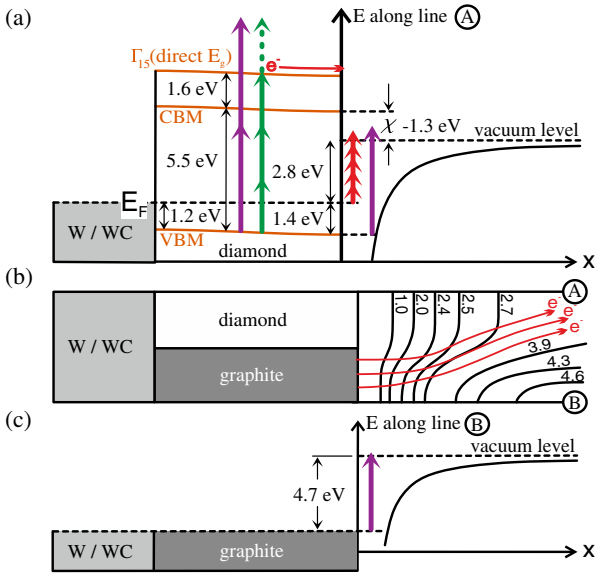

FIG. 4. Sketch of the relevant energy levels and optical excitation paths in the nanodiamond needle tip coating, including the graphitic boundaries. The concatenated arrows indicate excitation channels we identify as relevant here. The length and color of the arrows in Figs. 4(a) and 4(c) represent the photon energies of 0.64 (near infrared), 2.4 (green), and 4.8 eV (near ultraviolet). With these photoexcitation channels, we can explain the observed laser power and wavelength dependence discussed around Figs. 2 and 3. Intriguingly, this emission channel identification, except for the assignment of the one-photon process in the UV, seems to result in a unique attribution in spite of the intricate level structure. The work function of diamond is 2.8 eV for a negative electron affinity of $\chi = -1.3$ eV. In the diamond bulk, electrons can be excited across the indirect (5.5 eV) or direct band gap (7.1 eV), with two ultraviolet or three green photons, migrate to the surface, and cross the surface into vacuum. Alternatively, electrons can be excited into vacuum directly by one ultraviolet or five infrared photons. Even if the electrons originate from graphite close to the diamond interface, they effectively feel the work function of diamond, as indicated by their trajectories across the equipotential lines in Fig. 4(b). See text for details.

where we inserted −1.3 eV for the electron affinity of a fully hydrogen-terminated diamond surface [29,35]. The diamond work function also constitutes the low energy threshold for electrons originating from graphite [see Fig. 4(b)].

Based on this band diagram, we can identify electron emission channels with different energy thresholds, as indicated in Fig. 4(a). For diamond with negative electron affinity, the energy barrier between the conduction band minimum (CBM) at the surface does not exist: Electrons can be excited into the conduction band across the indirect (5.5 eV [36]) and direct band gaps (7.1 eV [37,38]), migrate to the surface, and escape straight into vacuum even if they have thermalized to CBM. Alternatively, direct optical excitation from electronic states at the surface to the plane-wave-like states in vacuum can lead to photoelectrons as well.

The emission probabilities of the different channels are complex functions of the densities of initial and final states, the number of photons necessary to provide the transition energy, and the laser intensity. We discuss them by referring to their signature in the $\log(J)$ vs $\log(I_p)$ plots in Figs. 2 and 3. Excitation with 1932 nm [$\hbar\omega = 0.64$ eV; red arrows in Fig. 4(a)] and observed photon order 5 can be identified as transitions at the surface from the Fermi level to the vacuum level. For clearer presentation, we have sketched the red arrows only in Fig. 4(a), although the initial states at the Fermi level can be assigned either to defects in the diamond or, more likely, to the graphitic grain boundaries [27].

At 512 nm ($\hbar\omega = 2.4$ eV; green arrows in Fig. 4), the effective nonlinearity equals 3.4, which we attribute to excitation across the direct band gap by three or by four photons.

With UV excitation ($\lambda < 350$ nm and $\hbar\omega > 3.5$ eV; violet arrows in Fig. 4), we observe one- and two-photon processes [Figs. 2(b) and 3]. We assign the one-photon process at low intensities to excitation at the surface from the Fermi level or the diamond VBM to the vacuum level. Evaluating energy differences only, the two-photon process ($\Delta E > 7.2$ eV for $\lambda < 350$ nm) could be assigned to all transitions in the band diagram of Fig. 4. We suggest, for this process, the transition across the direct band gap of diamond: The spatial overlap of the wave functions, the direct nature of the transition, and the large excitation volume make this process, by far, the most likely. This argument is supported also by the nonlinearity of 3.4, which we observe for 512 nm ($\hbar\omega = 2.4$ eV): Two photons of that energy would suffice to excite electrons from the VBM directly into vacuum. Nevertheless, this channel is not observed as the dominant one. The situation is different for 1932 nm ($\hbar\omega = 0.64$ eV): With this wavelength, excitation across the indirect band gap would require 9 photons and 11 photons across the direct band gap. These extremely high order processes are so unlikely that we observe the fifth order process at the surface as the dominant channel instead. For the spectral range investigated, we find no evidence of absorption across the indirect band gap as the dominant mechanism.

Lastly, we characterize the photoemission stability over time at different bunch charges and estimate the normalized peak brightness $B_{p,\mathrm{norm}}$. For the best comparison of $B_{p,\mathrm{norm}}$ with existing literature on ultrafast tip-shaped electron sources [8,9], we calculate all quantities as normalized root-mean-squared (rms) values and use the following definition:

$$B_{p,\mathrm{norm}} = \frac{J_p}{4\pi^2 \varepsilon_{x,\mathrm{norm}} \varepsilon_{y,\mathrm{norm}}}, \tag{3}$$

where J_p is the peak current, ε_i are the transverse emittances, and the subscript "norm" indicates normalized values. As an upper bound for the transverse emittances, we measure the emission angles α_i and we assume homogeneous emission across the geometrical radius of the emitter ($r = 170$ nm, $r_{\mathrm{rms}} = r/\sqrt{3}$). Note that the effective source size, and therefore the emittance of tip-shaped emitters, can be an order of magnitude smaller because the curved surface induces correlations between the origin and transverse momentum [16,39]. Photoemission at 1932 nm and 40 eV electron energy yields $\alpha_x = 0.16(6)$ rad, $\alpha_y = 0.15(9)$ rad, $\varepsilon_{x,\mathrm{norm}} = 0.20$ nm rad, and $\varepsilon_{y,\mathrm{norm}} = 0.19$ nm rad. Assuming that the emission duration matches the laser pulse duration, we calculate the normalized rms peak brightness of $B_{p,\mathrm{norm}} = 1.2 \times 10^{12}$ A m^{-2} sr^{-1} for one electron per pulse, which is comparable to a femtosecond cold field emitter at 15 electrons per pulse [9]. Because we use the geometrical and not the effective source size, and because we consider currents of one electron per pulse, we consider this peak brightness a lower bound.

The photoemitted current is stable over a timescale of at least half an hour at 256, 512, and 1932 nm with bunch charges of 55, 32, and 0.75 electrons per pulse, respectively (Fig. 5). With a stable 80 MHz Ti:Sa oscillator, the photocurrent is stable over more than 12 h and trillions of pulses. In contrast, the photoemission from an uncoated monocrystalline [310]-oriented tungsten tip decays over time (Fig. 5); a comparable behavior with even stronger decay was observed in a transmission electron microscope ($\hbar\omega = 2.4$ eV, $p = 1 \times 10^{-9}$ Pa [9]). Schottky emitters in scanning electron microscopes ($\hbar\omega = 3.6$ eV with reduced barrier height $\Phi_{\mathrm{eff}} = 1.6$ eV [5], and $\hbar\omega = 4.7$ eV with $\Phi_{\mathrm{eff}} = 2.8$–$3$ eV and $p < 4 \times 10^{-8}$ Pa [10]) show a similar behavior. Hence, nanodiamond-coated tungsten tips are more stable than these emitters: especially at low photon energies. (Working with low photon energies can be advantageous because the field enhancement at the apex [40] in combination with the nonlinearity enhances forward emission.)

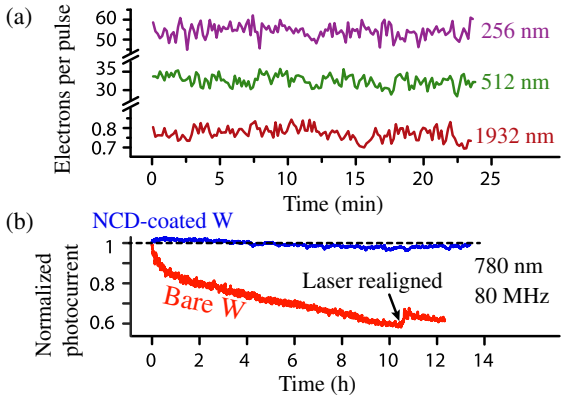

FIG. 5. (a) Photoemission at 1 kHz repetition rate is stable at 256, 512, and 1932 nm from the UV to the infrared, both below and above one electron per pulse. The noise is caused by laser power and pointing fluctuations. (b) Long-term photoemission at 80 MHz and 780 nm is stable from a diamond-coated tungsten tip (blue) and unstable from a bare tungsten tip (red). The short-term fluctuations (over 1 min) from the coated and uncoated tips are 3 and 5%; and the bunch charges at $t = 0$ are 25 and 6.5 electrons per pulse, respectively.

In dc field emission, occasional jumps occur, which is typical for cold field emission. The angular distribution in this emission mode is even smaller as compared to laser-induced emission.

We did not observe a change in laser-induced emission behavior during our experiments, with a laser fluence up to 30 mJ/cm^2 and 3.4×10^{11} W/cm^2 peak intensity. Hence, we find these as lower bounds of the damage threshold for diamond-coated tungsten tips. With 1932 nm pulses at 3.4×10^{11} W/cm^2, we have measured 400 electrons per pulse. At these large bunch charges, pulse broadening due to Coulomb repulsion is expected to be severe [10,41], which is why we have focused on smaller bunch charges.

In conclusion, we have presented femtosecond laser-induced electron emission from diamond-coated tungsten tips at 235–350, 512, 780, and 1932 nm. Based on the involved junctions between tungsten, diamond, and the graphitic grain boundaries, we have proposed an emission model that explains our experimental data well. Individual emission channels can be selected by proper choice of laser intensity and wavelength. These channels are identified by the number of photons needed to emit an electron. Stable photoelectron current and the high brightness of the emitted electrons are encouraging to further investigate diamond-coated tungsten tips as an ultrafast electron source.

Before resubmission of this Letter, we became aware of new and related work [42].

The authors acknowledge Mingjian Wu and Erdmann Spiecker for the transmission electron micrograph. They also acknowledge funding from the Deutsche Forschungsgemeinschaft via Grant No. SFB 953 titled "Synthetic Carbon Allotropes," from the European Research Council through the grant titled "Near Field Atto," and the Gordon and Betty Moore Foundation via Grant No. GBMF4744 titled "Accelerator on a Chip International Program-ACHIP."

*alexander.tafel@fau.de

[1] J. C. H. Spence, *High-Resolution Electron Microscopy*, 4th ed. (Oxford University, New York, 2013).
[2] O. Bostanjoglo, R. Elschner, Z. Mao, T. Nink, and M. Weingärtner, Ultramicroscopy **81**, 141 (2000).
[3] A. H. Zewail, Science **328**, 187 (2010).
[4] A. Arbouet, G. M. Caruso, and F. Houdellier, in *Advances in Imaging and Electron Physics* (Elsevier, New York, 2018), pp. 1–72.
[5] D.-S. Yang, O. F. Mohammed, and A. H. Zewail, Proc. Natl. Acad. Sci. U.S.A. **107**, 14993 (2010).
[6] D. A. Plemmons, P. K. Suri, and D. J. Flannigan, Chem. Mater. **27**, 3178 (2015).
[7] J. Sun, V. A. Melnikov, J. I. Khan, and O. F. Mohammed, J. Phys. Chem. Lett. **6**, 3884 (2015).
[8] A. Feist, N. Bach, N. R. da Silva, T. Danz, M. Möller, K. E. Priebe, T. Domröse, J. G. Gatzmann, S. Rost, J. Schauss, S. Strauch, R. Bormann, M. Sivis, S. Schäfer, and C. Ropers, Ultramicroscopy **176**, 63 (2017).
[9] F. Houdellier, G. Caruso, S. Weber, M. Kociak, and A. Arbouet, Ultramicroscopy **186**, 128 (2018).
[10] M. Kozák, J. McNeur, N. Schönenberger, J. Illmer, A. Li, A. Tafel, P. Yousefi, T. Eckstein, and P. Hommelhoff, J. Appl. Phys. **124**, 023104 (2018).
[11] P. Hommelhoff, Y. Sortais, A. Aghajani-Talesh, and M. A. Kasevich, Phys. Rev. Lett. **96**, 077401 (2006).
[12] P. Hommelhoff, C. Kealhofer, and M. A. Kasevich, Phys. Rev. Lett. **97**, 247402 (2006).
[13] B. Barwick, C. Corder, J. Strohaber, N. Chandler-Smith, C. Uiterwaal, and H. Batelaan, New J. Phys. **9**, 142 (2007).
[14] M. Krüger, M. Schenk, and P. Hommelhoff, Nature (London) **475**, 78 (2011).
[15] M. Bionta, B. Chalopin, J. Champeaux, S. Faure, A. Masseboeuf, P. Moretto-Capelle, and B. Chatel, J. Mod. Opt. **61**, 833 (2014).
[16] S. Meier, T. Higuchi, M. Nutz, A. Högele, and P. Hommelhoff, Appl. Phys. Lett. **113**, 143101 (2018).
[17] C. Ropers, D. R. Solli, C. P. Schulz, C. Lienau, and T. Elsaesser, Phys. Rev. Lett. **98**, 043907 (2007).
[18] R. Bormann, M. Gulde, A. Weismann, S. V. Yalunin, and C. Ropers, Phys. Rev. Lett. **105**, 147601 (2010).
[19] L. Wimmer, G. Herink, D. R. Solli, S. V. Yalunin, K. E. Echternkamp, and C. Ropers, Nat. Phys. **10**, 432 (2014).
[20] M. R. Bionta, S. J. Weber, I. Blum, J. Mauchain, B. Chatel, and B. Chalopin, New J. Phys. **18**, 103010 (2016).
[21] C. Kealhofer, S. M. Foreman, S. Gerlich, and M. A. Kasevich, Phys. Rev. B **86**, 035405 (2012).
[22] M. Bionta, B. Chalopin, A. Masseboeuf, and B. Chatel, Ultramicroscopy **159**, 152 (2015).
[23] C. Li, X. Zhou, F. Zhai, Z. Li, F. Yao, R. Qiao, K. Chen, M. T. Cole, D. Yu, Z. Sun, K. Liu, and Q. Dai, Adv. Mater. **29**, 1701580 (2017).

[24] V. Porshyn, V. I. Kleshch, E. A. Obraztsova, A. L. Chuvilin, D. Lützenkirchen-Hecht, and A. N. Obraztsov, Appl. Phys. Lett. **110**, 182101 (2017).
[25] J. B. Cui, M. Stammler, J. Ristein, and L. Ley, J. Appl. Phys. **88**, 3667 (2000).
[26] F. J. Himpsel, J. A. Knapp, J. A. VanVechten, and D. E. Eastman, Phys. Rev. B **20**, 624 (1979).
[27] J. B. Cui, J. Ristein, and L. Ley, Phys. Rev. B **60**, 16135 (1999).
[28] F. Maier, J. Ristein, and L. Ley, Phys. Rev. B **64**, 165411 (2001).
[29] J. B. Cui, J. Ristein, and L. Ley, Phys. Rev. Lett. **81**, 429 (1998).
[30] C. F. Davidson, G. B. Alexander, and M. E. Wadsworth, Metall. Mater. Trans. B **9**, 553 (1978).
[31] A. Tafel, M. Wu, E. Spiecker, P. Hommelhoff, and J. Ristein, Diam. Relat. Mater. **97**, 107446 (2019).
[32] J. B. Cui, J. Ristein, and L. Ley, Phys. Rev. B **59**, 5847 (1999).
[33] H. Shiomi, H. Nakahata, T. Imai, Y. Nishibayashi, and N. Fujimori, Jpn. J. Appl. Phys. **28**, 758 (1989).
[34] R. F. Willis, B. Fitton, and G. S. Painter, Phys. Rev. B **9**, 1926 (1974).
[35] J. Cui, J. Ristein, M. Stammler, K. Janischowsky, G. Kleber, and L. Ley, Diam. Relat. Mater. **9**, 1143 (2000).
[36] P. Dean, E. Lightowlers, and D. Wight, Phys. Rev. **140**, A352 (1965).
[37] F. Giustino, S. G. Louie, and M. L. Cohen, Phys. Rev. Lett. **105**, 265501 (2010).
[38] S. Logothetidis, J. Petalas, H. M. Polatoglou, and D. Fuchs, Phys. Rev. B **46**, 4483 (1992).
[39] D. Ehberger, J. Hammer, M. Eisele, M. Krüger, J. Noe, A. Högele, and P. Hommelhoff, Phys. Rev. Lett. **114**, 227601 (2015).
[40] S. Thomas, G. Wachter, C. Lemell, J. Burgdörfer, and P. Hommelhoff, New J. Phys. **17**, 063010 (2015).
[41] B. Cook and P. Kruit, Appl. Phys. Lett. **109**, 151901 (2016).
[42] M. Borz, M. H. Mammez, I. Blum, J. Houard, G. D. Costa, F. Delaroche, S. Idlahcen, A. Haboucha, A. Hideur, V. I. Kleshch, A. N. Obraztsov, and A. Vella, Nanoscale **11**, 6852 (2019).